Tribology International 117 (2018) 272–282

Contents lists available at ScienceDirect

Tribology International

journal homepage: www.elsevier.com/locate/triboint

Enhanced performance of optimised partially textured load bearing surfaces

R. Rahmani *, H. Rahnejat

Wolfson School of Mechanical, Electrical and Manufacturing Engineering, Loughborough University, Leicestershire, UK

ARTICLE INFO

Keywords:
Textured surfaces
Texture optimisation
Load carrying capacity
Viscous friction
Sliding contacts

ABSTRACT

Textured surfaces have been shown to provide enhanced tribological performance in a variety of contacts. Numerical analysis and optimisation methods are combined for application-oriented texture optimisation. However, an analytical approach is advantageous in providing more generic in-depth understanding of the nature of the relationships between texture parameters and objective functions, such as enhanced load carrying capacity and reduced friction. The paper outlines such an approach to obtain a set of global optimum design parameters for partially textured surfaces. The optimised results are expressed in dimensionless form, which enables their use for a variety of applications. The performance of optimised partially textured sliding surfaces is compared with the other conventional bearing geometries in their optimum state.

1. Introduction

Surface textures introduced on contacting surfaces act as micro-reservoirs of lubricant under operating conditions which do not otherwise yield a coherent film of lubricant. Such conditions include, inter alia, poor contact kinematics as in stop-start and reciprocating motions, high contact loads and poor conjunctional geometrical profiles. Surface textures create micro-wedges, acting as micro-bearings on their own accord. There has been an increasing volume of research on tribological performance of textured surfaces since the late 1990's [1,2] due to the advances made in their relatively cost-effective manufacture. These include laser surface texturing (LST) [3–7], which has attracted much interest. Owing to the diversity of load bearing conjunctions and operating conditions, there has been a plethora of reported research focused on particular applications such as journal bearings [8–11], thrust bearings [12,13], piston ring and cylinder liners [4–6,14,15], mechanical seals [1,2,16] and rolling element bearings [17,18] among other cases. There have also been studies on optimisation of the textured surfaces for specific applications [19]. However, due to a relatively large number of texture design parameters and operational conditions, a unified set of guidelines for the optimisation process for any given application has not hitherto emerged despite several in-depth contributions [20–23].

Rahmani et al. [24,25] proposed an analytical approach for investigation of tribological performance of partially textured sliding surfaces under hydrodynamic regime of lubrication. The objectives were to maximise hydrodynamic load carrying capacity and minimise viscous friction or the required flow rate. Their results provided a set of local optima, where for a given texture length ratio an optimum set of textured length and depth ratios could be specified for any given number of texture features. Alternatively, optimum values of texture length and depth ratios could be determined for a given number of textures at various texture length ratios. These characteristic ratios are defined in Section 2.

The advantage of the analytical approach is in providing an in-depth understanding of the relationships between the texture design parameters and stated measures of performance. Therefore, the underlying physical relationships can be readily obtained through an analytical approach. In addition, analytical solutions provide time-efficient solutions when compared with the numerical computations, using iterative techniques. The inherent error in the numerical method is also a factor that originates from its approximate nature. The advantage of numerical approach is dealing with complex geometries or those caused by any thermo-elastic effects. Furthermore, more complex texture shapes or patterns may be studied using numerical approaches.

The current study builds upon the analytical approach in Ref. [25] to provide a global set of optimum parameters, which would maximise the attainable load carrying capacity. It also provides a comparison between the performance of textured surfaces with other commonly used slider geometries, all with their optimum design; wherever analytically feasible.

2. Geometrical features of a textured contact

Fig. 1 shows a two-dimensional schematic representation of a textured sliding surface. The parameters used to characterise a textured

* Corresponding author.
E-mail address: R.Rahmani@lboro.ac.uk (R. Rahmani).

https://doi.org/10.1016/j.triboint.2017.09.011
Received 12 July 2017; Received in revised form 5 September 2017; Accepted 12 September 2017
Available online 18 September 2017

surface are: (i)- the number of textures, (ii)- the location of the textured area within the overall contact, (iii)- geometrical properties of texture features including their cross-sectional profile, maximum depth and width, and (iv)- the axial interspatial spacing between successive textures (pitch).

Using the notations in Fig. 1, the following dimensionless parameters are defined [26,27]:

- Texture depth ratio: This is the ratio of the maximum to the minimum gap between the counter face surfaces.

$$\xi = \frac{h_m + h_d}{h_m} = 1 + \frac{h_d}{h_m} \tag{1}$$

- Leading and trailing edge ratios: These are the ratios of the leading and the trailing edges of the textured region to the overall bearing axial length:

$$\alpha_0 = \frac{l_0}{L},\ \alpha_n = \frac{l_n}{L} \tag{2}$$

- Texture length ratio: This is the ratio of the texture length at the base to the interspatial space between successive texture features:

$$\varepsilon = \frac{d_x}{l_x} \tag{3}$$

- Textured length ratio: This is the ratio of the length of textured area to the overall bearing axial length:

$$\kappa = 1 - (\alpha_0 + \alpha_n) \tag{4}$$

3. Governing relationships

Reynolds equation is commonly used to model lubricated conjunctions comprising textured surface(s). To model textured features of finite lateral width (e.g. pores or chevrons), a two-dimensional form of Reynolds equation should be used, along with numerical solution techniques such as finite difference methods in order to obtain the generated pressure distribution [26,28]. For cases where the lateral texture widths may be considered large in comparison with their lengths, use of one-dimensional Reynolds equation is justified as in the case of infinite-width micro-bearings. Consequently, explicit analytical relationships for load carrying capacity and viscous friction can be derived and used to calculate the tribological performance of the given textured contact. As a result, a thorough parametric study can be conducted, through which the optimum geometrical parameters for the texture features may be determined. In such an approach, the extent to which any performance criterion may be influenced by any chosen design parameter can be ascertained. This enables the designers to identify design features with a greater degree of confidence, as well as identify the underlining physical principles.

The analytical methodology and associated boundary conditions are specified in Rahmani et al. [25–27] in some detail. The current analysis assumes an incompressible lubricant under iso-viscous condition. In addition, it is assumed that there is negligible thermal gradient in the contact domain. This is generally the case in many applications including for piston rings and cylinder liner conjunction [29], big-end bearings [30] and ball bearings [31]. Therefore, an average effective contact temperature may be assumed. The dimensionless relationships provided in Refs. [25–27] are independent of the lubricant viscosity. Therefore, when converting the results into dimensional parameters such as load carrying capacity and friction an adjusted lubricant viscosity for the contact operating temperature can be used. Furthermore, the current study is a comparative study of texture parameters for contact conjunctions which are assumed to be subjected to the same operating conditions in each studied case, with the differences accounting for the various texture parameters.

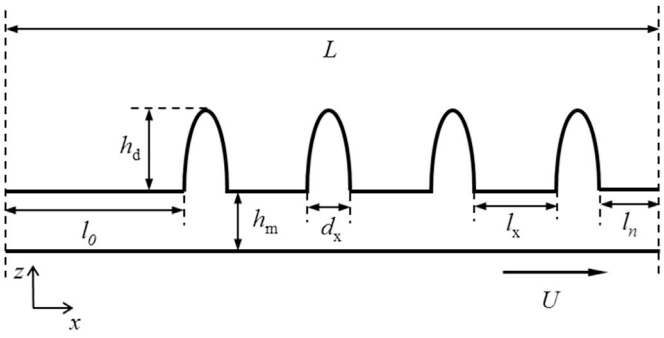

Fig. 1. Schematic of a textured contact subject to sliding motion and corresponding geometrical parameters.

The analytical relationships provided in Ref. [25] for textures of rectangular and isosceles triangular profiles are used in the current study. For clarity, these relationships are restated here.

The dimensionless performance parameters in terms of load carrying capacity and friction are defined as:

$$\Lambda_w = W \frac{1}{\eta U} \left(\frac{h_m}{L}\right)^2 \tag{5}$$

and

$$\Lambda_f = f \frac{1}{\eta U} \left(\frac{h_m}{L}\right) \tag{6}$$

where, W and f are load carrying capacity and friction per unit lateral width of the contact. In addition, η and U represent lubricant dynamic viscosity and sliding speed respectively, while h_m and L denote the minimum film thickness and the overall contact length (in the axial direction).

The ratio of dimensionless friction to dimensionless load carrying capacity is indicative of the coefficient of friction when it is purely based on texture geometrical parameters:

$$\Omega = \frac{\Lambda_f}{\Lambda_w} = \frac{f}{W}\frac{L}{h_m} = \mu\left(\frac{L}{h_m}\right) \tag{7}$$

As it can be seen Ω is a scaled-up representation of the coefficient of friction, μ, by the ratio of contact length over the minimum film thickness. Hereinafter, Ω is referred to as scaled coefficient of friction and is used in the comparison of numerical results of various bearing configurations later in Section 4.

In the case of rectangular shape texture features the dimensionless load carrying capacity and friction become:

$$\Lambda_w = \frac{3m\varepsilon\kappa(1-\kappa)(\xi-1)}{(m+\xi-1)\xi^3 - m\varepsilon\kappa\left(\xi^3-1\right)} \tag{8}$$

$$\Lambda_f = \frac{m^2\varepsilon^2\kappa^2(\xi-1)^4 + \xi(m+\varepsilon-1)\left[(m+\xi-1)\xi^3 - 2m\varepsilon\kappa(\xi-1)\left(\xi^2-\xi+2\right)\right]}{\xi(m+\varepsilon-1)\left[(m+\varepsilon-1)\xi^3 - m\varepsilon\kappa\left(\xi^3-1\right)\right]} \tag{9}$$

For the case of triangular shape texture features, the corresponding dimensionless load carrying capacity and friction are:

$$\Lambda_w = \frac{3m\varepsilon\kappa(1-\kappa)(\xi-1)}{2(m+\xi-1)\xi^2 - m\varepsilon\kappa(2\xi+1)(\xi-1)} \tag{10}$$

$$\Lambda_f = \frac{4m\varepsilon\kappa}{(\xi-1)(m+\varepsilon-1)}\ln\xi + \frac{2\{(m+\varepsilon-1)[(m+\varepsilon-1)\xi^2 - 2m\varepsilon\kappa(\xi^2+2\xi-1)] + m^2\varepsilon^2\kappa^2(\xi+5)(\xi-1)\}}{(m+\varepsilon-1)[2(m+\varepsilon-1)\xi^2 - m\varepsilon\kappa(2\xi^2-\xi-1)]} \tag{11}$$

In the above relationships, it is assumed that the trailing edge ratio, α_n, is diminutive since it has a negligible effect. Therefore, it can be ignored in the evaluation of bearing performance.

The above relationships can be used for design purposes as well. It is important to note that the results from the current study are only applicable for a prevalent hydrodynamic regime of lubrication (i.e., $\lambda = h_m/\sigma > 3$). Therefore, for a given load, texture population and distribution, texture depth ratio can be calculated through either of equations (8) and (10). Subsequently, the minimum required texture depth can be calculated through: $h_d = 3(\xi-1)\sigma$. If it is decided to operate at higher minimum film thickness values, then the required texture depth should proportionally increase, based on this relationship, in order to maintain the same load carrying capacity. Conversely, there exists a limit on amount of increase in the minimum film thickness for the above relationships to hold true. This limit is imposed by the assumptions made, based on which Reynolds equation is derived and remains valid for use; i.e. $(h_d + h_m)/L < O(10^{-3})$.

4. Optimisation process for rectangular and triangular textured surfaces

The above stated analytical relations enable the determination of optimum texture parameters to achieve maximum load carrying capacity or minimum friction. Examining the relations shows that load carrying capacity reduces monotonically with number of textures, m, and increases with the texture length ratio, ε. Therefore, specific optimum conditions cannot be obtained through derivatives of load carrying capacity with respect to either m or ε. However, there would exist specific values for κ or ξ, based on which the load carrying capacity may be maximised. Nevertheless, these values would be a function of number of textures and texture length ratio, for any given texture shape.

To obtain the global maximum for load carrying capacity, the root of equation $\partial\Lambda_w/\partial\kappa = 0$ would provide positive values of κ, which can be substituted back into the corresponding Λ_w term and differentiated again with respect to ξ. Solving the resulting equation provides the global ξ_{opt} values. In this process roots that provide negative or imaginary values are discarded. Replacing ξ_{opt} into the equation for κ provides the global κ_{opt} values. In addition, replacing these parameters back into the equation for Λ_w provides a relationship for the global $(\Lambda_w)_{max}$. Due to the tedious nature of the problem, the whole process is carried out in a Computer Algebra System (CAS) software. The same procedure can also be carried out when dealing with the minimisation of friction as an objective function. It is also important that the roots obtained are re-examined through the use of the second derivative, ensuring that they represent the correct extremum values.

Taking into account both of these global optima; ξ_{opt} and κ_{opt} together, the resulting load carrying capacity can be considered as the global rather than the local maximum.

A further clarification on the concept of global as opposed to localised optima is instructive at this point. If, for example, in the above stated relations, a variable (e.g. κ) remains constant, then the value of ξ, resulting in the maximum load carrying capacity (as the objective function) can be considered as a localised extremum. The determined value of the objective function is thus regarded as a local maximum. However, when searching for the global maximum, the optimum for the effects of both variables (i.e. κ and ξ) is sought.

Unlike for load carrying capacity, no specific extremum point for friction can be found based on any of the defined texture parameters. In this case, the obtained roots of the derivative functions prove to be inflexion points. Examining the corresponding relationships for the defined scaled coefficient of friction reveals the existence of optima for κ and ξ similar to the case for Λ_w, however, this is not explored further in this study.

Following the foregoing approach, the optimisation for the global maximised load carrying capacity for both rectangular texture and triangular shaped textures can now be determined.

4.1. Optimisation of textures with rectangular shape

Fig. 2(a) and (b) show the global optimum values for κ and ξ, for the case of maximum load carrying capacity for different number of textures, m.

The results show that for maximum load carrying capacity for a bearing with flat end textures, it is desirable to confine the texture depth to 50%–80% of the anticipated minimum lubricant film thickness. Furthermore, the textured area should preferably cover 50%–72% of the apparent contact area. This is irrespective of the ratio of the texture length to the interspatial spacing between adjacent textures, as well as the number of textures.

Fig. 2(a) also shows that as the length of the texture features increase or their interspacing reduces, the size of the optimum textured area rises, until it reaches to almost three-quarters of the contact length. Fig. 2(b) shows the growth in the optimum texture depth as the texture length ratio increases, when the operating minimum lubricant film thickness remains unchanged.

Fig. 3(a) and (b) show the maximum attainable dimensionless load carrying capacity and the corresponding generated viscous friction.

Fig. 3(a) shows that the texture features of lengths comparable to their interspacing (i.e. with $\varepsilon \to 1$), produce the highest load carrying capacity, whilst keeping the generated friction to a minimum as seen in Fig. 3(b). In addition, the optima do not alter significantly with the number of textures, when $\varepsilon \to 1$. It also appears that lower number of textures result in improved hydrodynamic performance. This is indeed what one would expect as the maximum possible load carrying capacity would be represented by a Rayleigh-step bearing [32], which is based on the developed analytical methodology here corresponds to the case with $m = 1$, as $\alpha_n \approx 0$.

It must also be noted that at the other extreme, when $\varepsilon \to 0$ (i.e. the length of textures become much smaller than their interspatial distance), the dimensionless load carrying capacity tends to that of a smooth flat plate with no texture features. It is obvious that in such circumstances, the load carrying capacity would diminish and the coefficient of friction would theoretically tend to infinity. This condition corresponds to cessation of pressure perturbations resulting from micro-wedge effect of texture features, thus no hydrodynamic load carrying capacity. Morris et al. [6] have shown that micro-hydrodynamic lift occurs due to pressure perturbations at the leading edge of texture features in lubricant

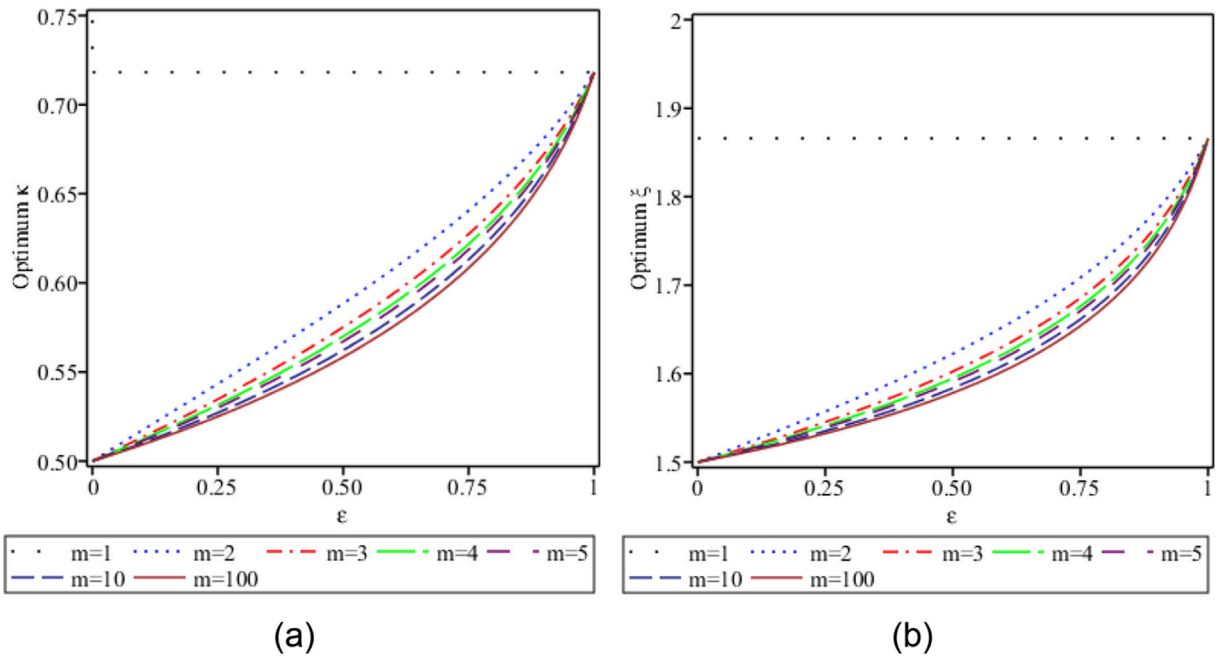

Fig. 2. Optimum values for (a) textured length ratio, and (b) for texture length ratio for different number of textures of rectangular shape.

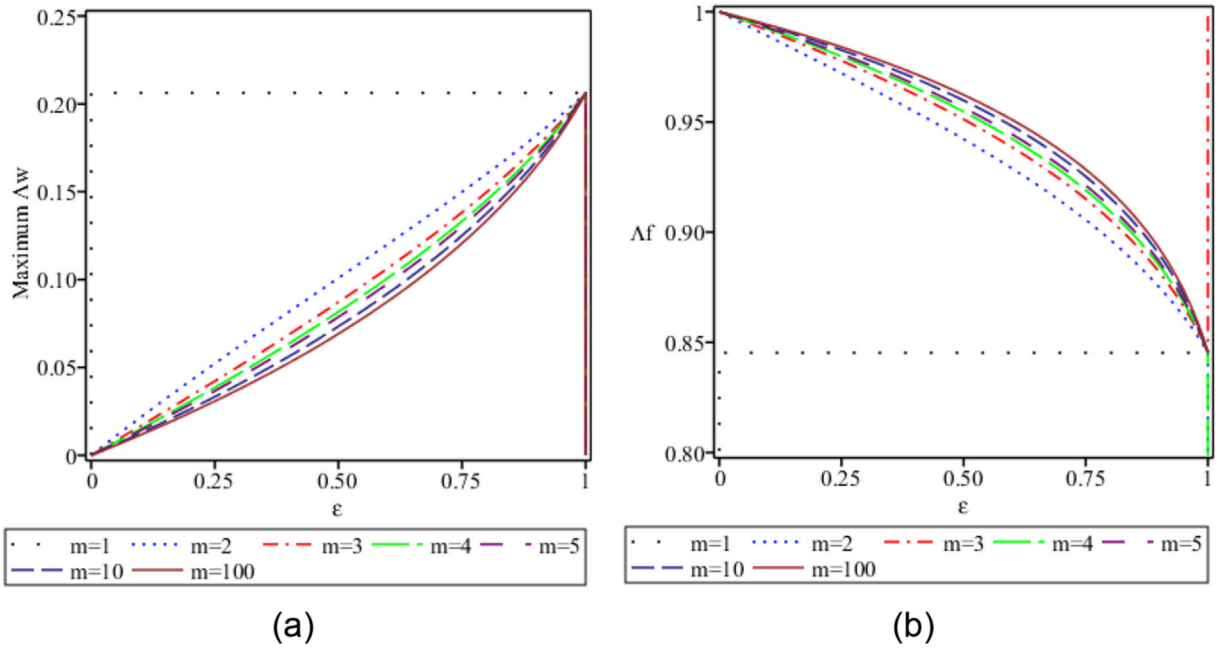

Fig. 3. (a) Maximum dimensionless load carrying capacity and the corresponding dimensionless friction for different number of rectangular-shaped textures.

4.2. Optimisation of textures with triangular shape

It is also possible to optimise textures of triangular profile in terms of values for κ and ξ, which would yield maximum load carrying capacity for any given number of textures. Fig. 4 shows the variations of κ and ξ for different number of textures and texture length ratios.

Compared with the case of rectangular textures, the optimum textured portion of the bearing surface is between 50% and 65% of the whole bearing length (Fig. 4(a)), which is slightly less than the case of rectangular-profiled textures. On the other hand, the optimum texture depths are considerably (~46% at $\varepsilon \cong 1$) larger (Fig. 4(b)) than the case of rectangular textures. This implies that triangular-shaped textures should be deeper in order to achieve highest possible hydrodynamic lift capacity.

The corresponding dimensionless maximum load carrying capacity and associated generated friction are shown in Fig. 5.

The trends in the results of Fig. 5 are quite similar to those already observed for the rectangular-shaped textures (Fig. 3). A relative comparison of the maximum attainable load carrying capacity for both rectangular and triangular textures shows the superior performance of the former. The flatness of the texture base and particularly the straightness of the side walls of rectangular textures appear to be the reason for this enhanced performance. The sharp geometrical gradient at the texture edges promotes micro-wedges (thus pressure perturbations) which are essential for high pressure film formation as determined by the term dh/dx in Reynolds equation. This comparative study also shows

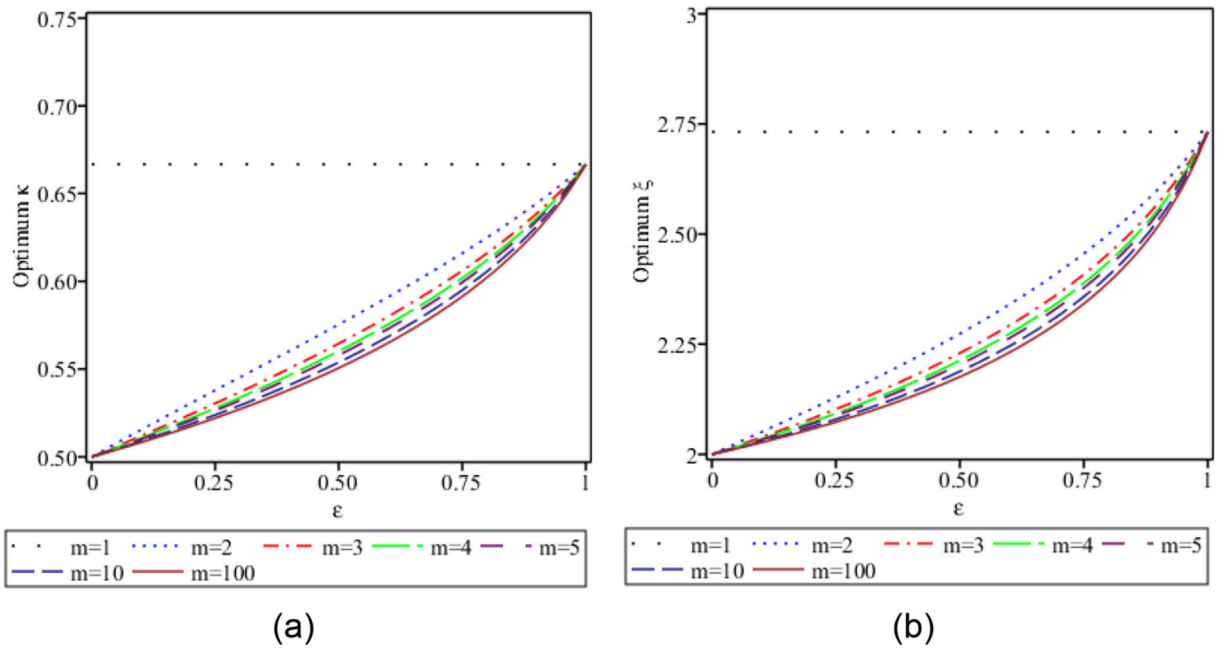

Fig. 4. Optimum values for: (a) textured length ratio and (b) texture ratio for different number of triangular-shaped texture features.

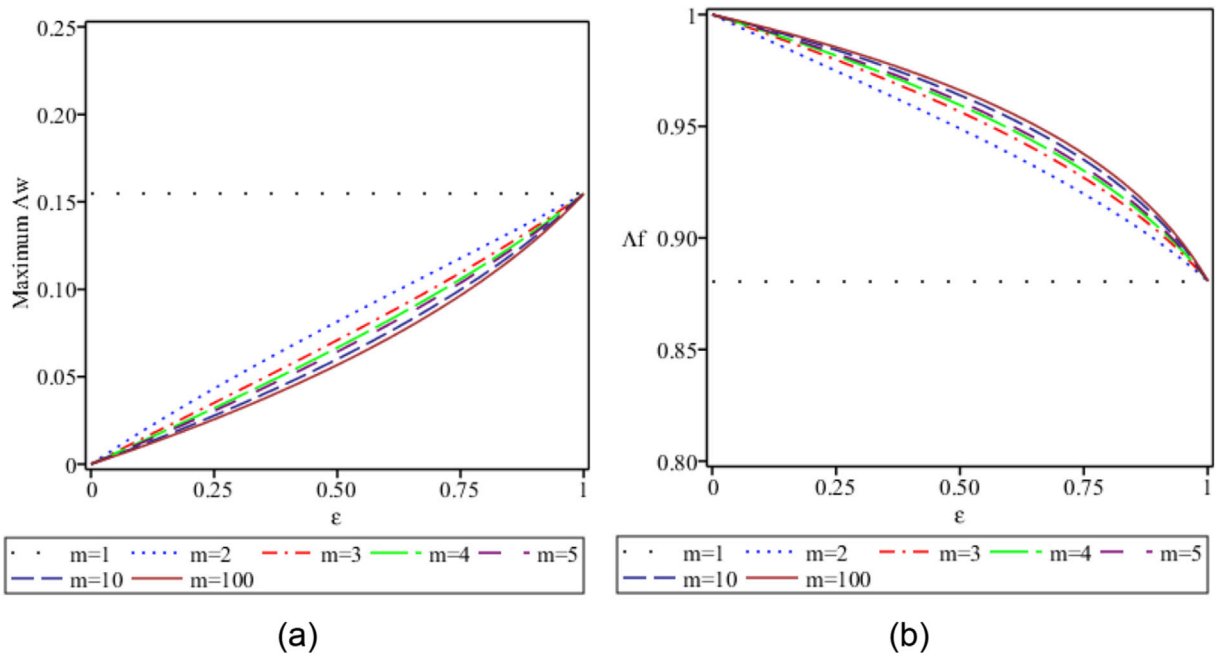

Fig. 5. (a) Maximum dimensionless load carrying capacity and (b) the corresponding dimensionless generated viscous friction for different number of triangular-shaped textures.

reduced friction in the case of rectangular-shaped textures.

4.3. Comparison of the coefficient of frictions

The results for the defined scaled coefficient of friction for both rectangular and triangular shape textures are shown in Fig. 6.

Considering the assumptions upon which Reynolds equation is based, it is essential to note that: $h_m/L \approx O(10^{-3})$ (or less) for validity of the results of analysis carried out here.

The results in Fig. 6 indicate that the minimum scaled coefficient of friction occurs, when: $\varepsilon \rightarrow 1$. At or around this texture length ratio, the effect of the actual number of textures becomes unimportant. It can also be seen that the optimised rectangular textures produce lower coefficient of friction compared with their triangular counterparts. These represent good guidelines for manufacture of textured surfaces in reducing costs and improving the throughput time in mass manufacturing environment.

5. Evaluating the performance of optimised fundamental slider profiles

To gauge the effectiveness of texturing, it seems appropriate to compare the performance of textured surfaces with other fundamental

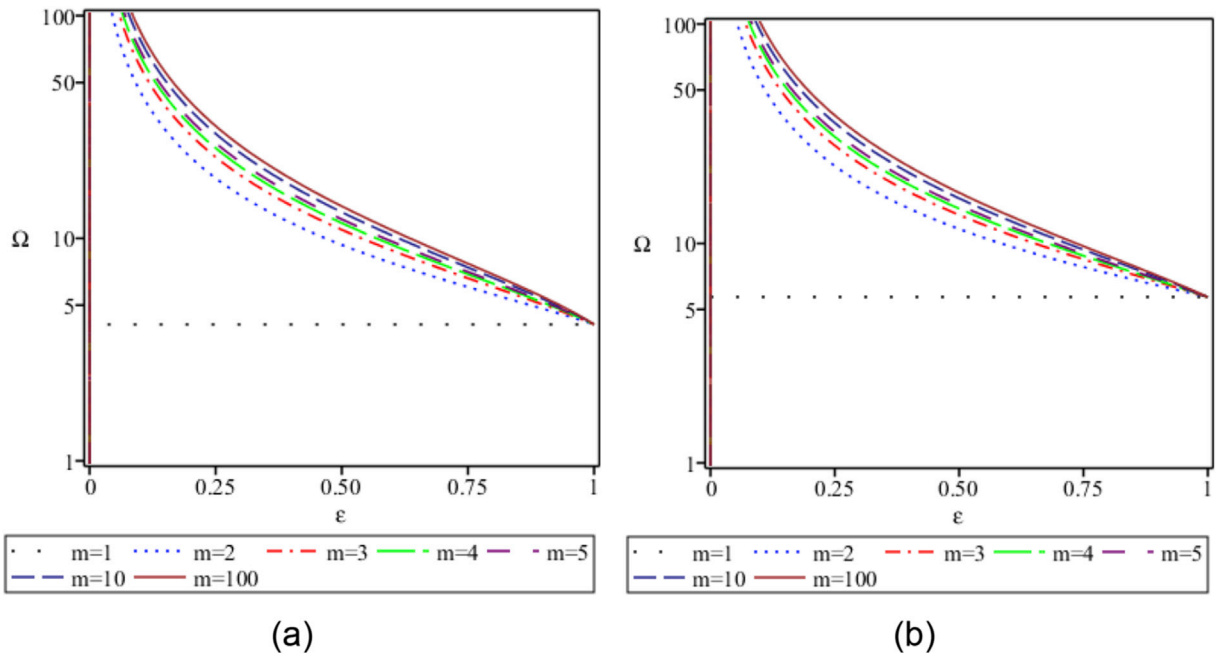

Fig. 6. Comparison of the scaled coefficient of friction for (a)-rectangular and (b)- triangular shaped textures.

and conventionally established bearing geometries.

5.1. Case of two sliding parallel flat plates

The case of lubricated contact of a smooth parallel flat slider of infinite width (requiring one-dimensional solution of Reynolds equation) is considered. For two parallel flat semi-infinite planes with a gap of h_m, in relative sliding motion and in the absence of any pressure gradient, no load carrying capacity would be generated as: $dh/dx = 0$. It should be noted that the effect of any viscous and thermal wedges are ignored here. Therefore, the performance of such contact can be evaluated as:

$$W = 0,\ f = \frac{\eta UL}{h_m}, \mu = \infty \tag{12}$$

Alternatively, in terms of the aforementioned dimensionless parameters (Section 2):

$$\Lambda_w = 0, \Lambda_f = 1, \Omega = \infty \tag{13}$$

5.2. Inclined pad bearing

For an inclined sliding pad bearing (Fig. 7), it is also possible to obtain the equivalent performance parameters in an optimised configuration.

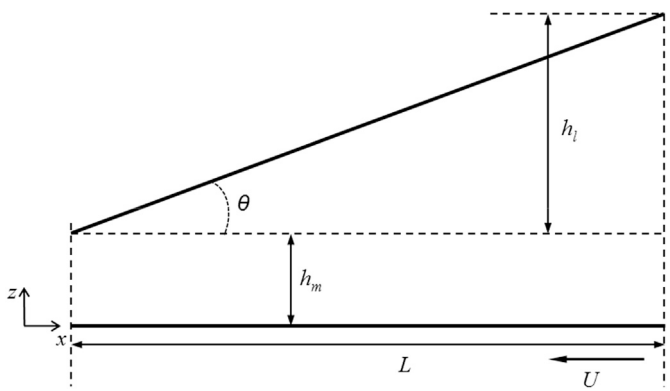

Fig. 7. Schematic of inclined pad bearing.

Following the same convention as before, the height ratio parameter can be defined as:

$$\xi = 1 + \frac{h_l}{h_m} \tag{14}$$

where, h_I is the maximum inclination height.

In the absence of any pressure differential between the inlet and outlet boundaries, the bearing performance parameters including its load carrying capacity and generated viscous friction in dimensionless form become [26]:

$$\Lambda_w = \frac{6\ln\xi}{(\xi-1)^2} - \frac{12}{\xi^2-1} \tag{15}$$

$$\Lambda_f = \frac{4\ln\xi}{\xi-1} - \frac{6}{\xi+1} \tag{16}$$

The optimum value for ξ to achieve the maximum load carrying capacity becomes: $(\xi_{opt})_{\max\Lambda_w} = 2.1887$, with the optimum inclination angle of:

$$\theta_{opt} = \tan^{-1}\left[(\xi_{opt}-1)\frac{h_m}{L}\right] \tag{17}$$

Using the obtained optimum value for the height ratio, the maximum dimensionless attainable load carrying capacity and the corresponding generated viscous friction, and the scaled coefficient of friction coefficient for this case become: $(\Lambda_w)_{max} = 0.1602$, $\Lambda_f = 0.7542$ and $\Omega = 4.7066$ respectively.

It is also possible to find the optimum value of ξ which would provide the minimum scaled coefficient of friction. The optimum value for ξ to achieve this, is: $(\xi_{opt})_{\min\Omega} = 2.5335$. Using this value, the corresponding dimensionless load carrying capacity becomes: $\Lambda_w = 0.1572$, whilst $\Lambda_f = 0.7268$ and $(\Omega)_{min} = 4.6223$.

5.3. The Rayleigh-step bearing

A comprehensive optimisation study of the Rayleigh-step bearing is

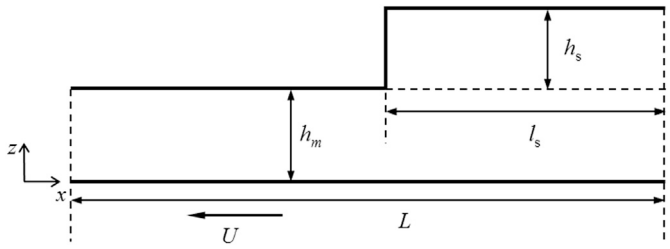

Fig. 8. Schematic of Rayleigh step bearing.

provided by Rahmani et al. [32]. Fig. 8 is a schematic representation of a Rayleigh step bearing.

The step ratio and the ratio of the step length to the overall bearing are defined as:

$$\xi = 1 + \frac{h_s}{h_m} \tag{18}$$

$$\kappa = \frac{l_s}{L} \tag{19}$$

The dimensionless load carrying capacity and the generated viscous friction become [32]:

$$\Lambda_w = \frac{3\kappa(\xi-1)(\kappa-1)}{\kappa\left(\xi^3-1\right)-\xi^3} \tag{20}$$

$$\Lambda_f = \frac{\kappa^2(\xi-1)^4 - 2\kappa\xi(\xi-1)\left(\xi^2-\xi+2\right)+\xi^4}{\xi\left[\xi^3-\kappa\left(\xi^3-1\right)\right]} \tag{21}$$

The maximum global load carrying capacity is obtained when $(\kappa_{opt})_{\max\Lambda_w} = 0.7182$ and $(\xi_{opt})_{\max\Lambda_w} = 1.866$. For these optimum values, the maximum dimensionless bearing load carrying capacity, the corresponding generated friction and the coefficient of friction are found to be: $(\Lambda_w)_{max} = 0.2063$, $\Lambda_f = 0.8453$ and $\Omega = 4.0981$, respectively.

For minimisation of coefficient of friction, the optimum values are calculated to be $(\kappa_{opt})_{\min\Omega} = 0.8$, and $(\xi_{opt})_{\min\Omega} = 2$. These values result in: $\Lambda_w = 0.2$, $\Lambda_f = 0.8$ and $(\Omega)_{\min} = 4$ respectively.

5.4. Parabolic converging-diverging profile

The parabolic conjunctional profile (Fig. 9) has a wide range of applications, particularly in the presence of relative sliding motion. A good example is the top compression ring of the internal combustion engine, where the ring is usually crowned with a parabolic profile. Morris et al. [33] studied the optimum converging-diverging profile for piston compression rings with a parabolic and other various power indices.

The parabolic profile is described as:

$$S = \frac{x^2}{2R} \tag{22}$$

where, R is the crown radius. The relationship between the crown radius, crown height and the ring contact face length is as [34]:

$$h_r = \frac{(L/2)^2}{2R} \tag{23}$$

Following the convention set earlier, the ring crown height ratio can be defined as:

$$\xi = 1 + \frac{h_r}{h_m} \tag{24}$$

Gohar and Rahnejat [35] provide the following relationship for load carrying capacity per unit lateral length of an infinite length parabolic converging-diverging profile in the absence of the squeeze film effect, when Swift-Stieber outlet boundary conditions are used:

$$W = 2.45R\left(\frac{\eta U}{h_m}\right) \tag{25}$$

which, using the definitions provided above can be represented in non-dimensional form as:

$$\Lambda_w \cong \frac{0.3063}{\xi-1} \tag{26}$$

However, it can be shown that for a finite length converging-diverging profile, taking into account the effect of cavitation with the Swift-Stieber lubricant rupture point and in the absence of the squeeze film effect, the load carrying capacity per unit lateral width alters. This is obtained in the Appendix, yielding:

$$\Lambda_w = -\frac{3}{8\xi^2\sqrt{\xi-1}}\left\{\bar{c}\xi^2\left[12\bar{c}^2(\xi-1)-1\right]\left[\tan^{-1}\left(2\bar{c}\sqrt{\xi-1}\right)+\tan^{-1}\left(\sqrt{\xi-1}\right)\right]+\sqrt{\xi-1}\,(2\bar{c}+1)\left[6\bar{c}^2\xi^2-2\bar{c}^2\,\xi-4\bar{c}^2+\bar{c}\xi-\xi+1\right]\right\} \tag{27}$$

where $\bar{c} = c/L$, in which c is the location of cavitation inception point as measured from the centre of the contact where: $x = 0$. In other words, the location of cavitation inception point as measured from the lubricant entrant point, in dimensionless form, becomes: $\kappa = 0.5 + \bar{c}$. This is the portion of the bearing length which experiences high pressures (i.e. length of the non-cavitated zone).

The value for $\bar{c}$ is obtained through implementation of Swift-Stieber boundary conditions as: $(\partial p/\partial x)_c = p(c) = 0$, and through numerical

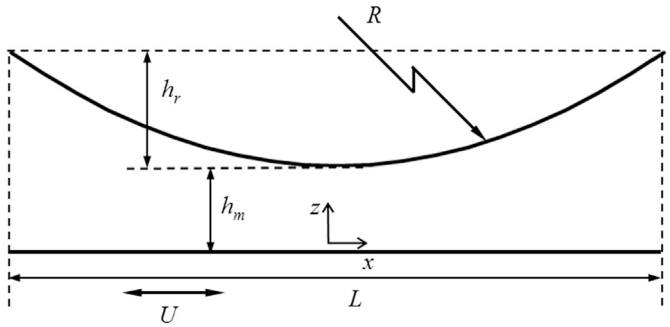

Fig. 9. Schematic of a converging-diverging symmetric parabolic contact profile.

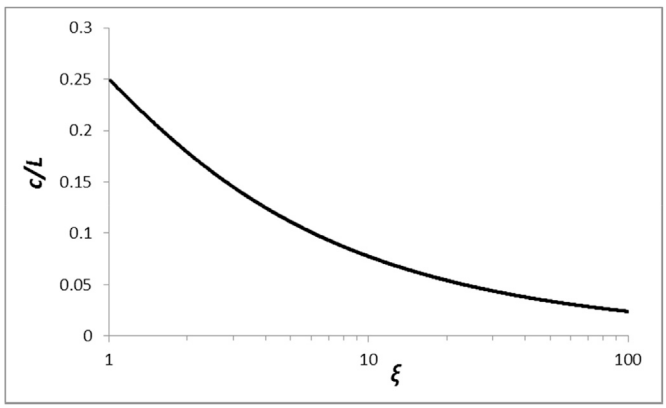

Fig. 10. Variation of location of cavitation inception point with ξ.

solution of the resultant non-linear equation:

$$\left[\tan^{-1}\left(2\bar{c}\sqrt{\xi-1}\right)-\tan^{-1}\left(-\sqrt{\xi-1}\right)\right]\frac{1-12(\xi-1)\bar{c}^2}{4\sqrt{\xi-1}} = \frac{1+4(\xi-1)\bar{c}^2}{2}\left(\frac{\bar{c}[12(\xi-1)\bar{c}^2+5]}{[4(\xi-1)\bar{c}^2+1]^2}+\frac{3\xi+2}{2\xi^2}\right) - \frac{4(\xi-1)\bar{c}^2+1+2\xi\bar{c}}{\xi(4(\xi-1)\bar{c}^2+1)} \quad (28)$$

Fig. 10 shows the variation of the location of film rupture (cavitation inception point) with ξ. Consequently, a relationship for determining the value of $\bar{c}$ for any given value of ξ in the range $1<\xi<100$, can be obtained through regression analysis of the numerical results as:

$$\bar{c} \cong 0.2523\xi^{-0.513} \quad (29)$$

Therefore, if the crown height remains below the minimum film thickness (i.e. $\xi<2$), then the cavitated region can cover 18–25% of the entire contact length. If on the other hand the crown height becomes greater than the minimum film thickness (i.e. $\xi>2$), then the cavitated region grows further in its extent.

Variation of Λ_w with ξ can now be obtained using the equation derived above for the dimensionless load carrying capacity. Fig. 11 shows the variation of dimensionless load carrying capacity with ξ.

As it can be seen, at the transition point, where the crown height is slightly larger than the minimum film thickness, the maximum possible load carrying capacity would be expected.

The optimum crown height ratio, which provides the maximum load carrying capacity, can then be obtained from the results of Fig. 11. The optimum value is: $(\xi_{opt})_{max\Lambda_w} \cong 2.193$, which yields: $(\Lambda_w)_{max} \cong 0.0657$. Thus, to gain maximum load carrying capacity from a parabolic profile in lubricated sliding motion, the ratio of the crown height to the minimum film thickness should be approximately 1.193.

Fig. 12 provides a comparison of the results for finite converging-diverging profile and that with the pressure boundaries set at infinity, representing a fully flooded conjunction. It can be seen that with reduced crown height-to-film thickness ratios the error becomes significant. Nevertheless, in the case of a piston top compression ring, where the ring crown height is typically 10–20 μm, if the lubricant minimum film thickness is considered to be typically 1~2 μm in the vicinity of dead-centre reversals, then: $\xi \approx 10$ and the difference in the predicted load carrying capacity would be less than 30%.

Using the definitions given above and also stated in the Appendix, the dimensionless friction is obtained as:

$$\Lambda_f = \frac{1}{4\xi\sqrt{\xi-1}}\left\{3\xi\left[4\bar{c}^2(\mp\xi\pm1)-1\right]\left[\tan^{-1}\left(\sqrt{\xi-1}\right)+\tan^{-1}\left(2\bar{c}\sqrt{\xi-1}\right)\right]+3\sqrt{\xi-1}\left[4\bar{c}^2(\mp\xi\pm1)+2\xi\bar{c}\mp1\right]+4\overline{U}\xi\tan^{-1}\left(\sqrt{\xi-1}\right)\right\} \quad (30)$$

where, the negative sign is used for the lower surface and the positive sign is for the upper surface in a sliding-pair contact. In addition, the term $\overline{U}=(U_2-U_1)/(U_2+U_1)$ can be used to characterise the slide-roll ratio in the contact of ellipsoidal solids of revolution as in rolling element bearings.

Using $(\xi_{opt})_{max\Lambda_w} \cong 2.193$, the values for dimensionless friction and the scaled coefficient of friction are obtained as $\Lambda_f = 0.699$ and $\Omega = 10.640$. In addition, the location of the lubricant film rupture becomes: $\bar{c} = 0.1687$.

Fig. 13, shows that viscous friction reduces rather monotonically with ξ and hence no particular optimum values can be stated. However, Fig. 14 shows that it is possible to obtain an optimum value for ξ which would provide the least attainable scaled coefficient of friction, using the devised relationship between the location of cavitation inception point and the crown height to the minimum film thickness ratio (equation (29)) stated earlier.

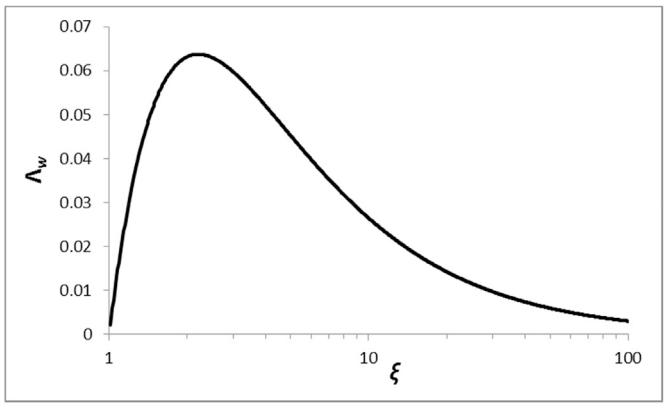

Fig. 11. Variation of dimensionless load carrying capacity for a finite length parabolic slider.

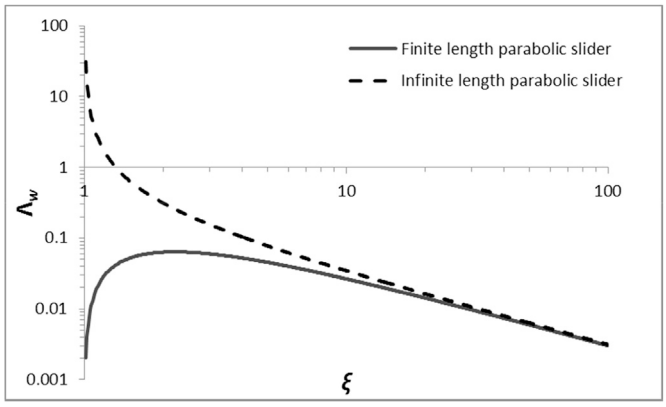

Fig. 12. Comparison of the load carrying capacity for finite converging-diverging profile and that with the pressure boundaries set at infinity.

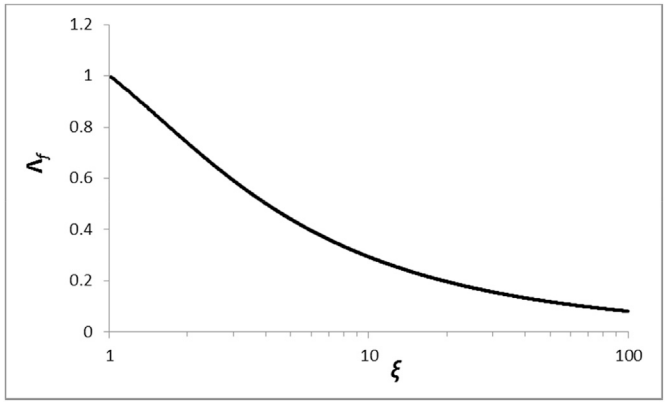

Fig. 13. Variations of dimensionless friction with defined height ratios for the parabolic contact profile.

The minimum value of scaled coefficient of friction is obtained for $(\xi_{opt})_{min\Omega} \cong 3.822$, with $(\Omega)_{min} \cong 9.425$ and $\Lambda_w \cong 0.0544$. In addition, the location of film rupture would be at: $\bar{c} = 0.1267$.

5.5. Comparison of various bearing profiles and partially textured surfaces

The results from the optimisation process based on maximising load carrying capacity are summarised in Table 1. As expected, the results show that the Rayleigh step bearing would provide the highest load

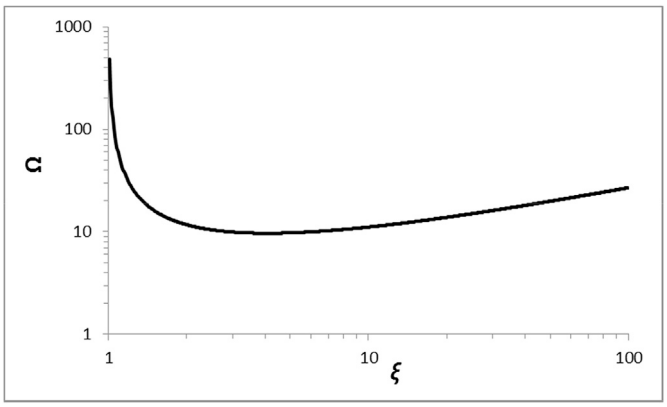

Fig. 14. Variation of scaled coefficient of friction with defined height ratio for the parabolic profile.

rectangular and triangular features is examined to obtain optimum texture characteristics for maximum load carrying capacity. The dimensionless approach yields feature parameters which are solely geometrical. The expounded approach provides an opportunity to isolate the influence of these parameters upon specified bearing measures of performance.

The analysis shows that the performance of a textured surface deteriorates as the number of features increases. This means that a Rayleigh-step bearing represents the ideal geometry for applications that it can be practically employed. Additionally, the textures with base lengths comparable with their interspatial spacing perform better for the chosen measures of performance (i.e. load carrying capacity and reduced friction). It was also concluded that the optimum performance is achieved when approximately two-thirds to three-quarters (depending on the feature shape) of overall contact domain is textured.

The optimum depth of texture in the case of rectangular features is approximately 80–85% of the predicted minimum lubricant film thickness, whilst in the case of triangular textures this should be 70–75%

Table 1
Comparison of performance for different slider bearing configurations.

	Flat plate	Inclined pad	Rayleigh step	Rectangular $m = 2$	Triangular $m = 2$	Rectangular $m = 10$	Triangular $m = 10$	Parabolic profile
ε_{opt}	–	–	–	0.9900-	0.9900	0.9900	0.9900	–
κ_{opt}	–	–	0.7182	0.7139	0.6643	0.7105	0.6624	0.6687
ξ_{opt}	–	2.1887	1.8660	1.8559	2.7173	1.8483	2.7060	2.1931
$(\Lambda_w)_{max}$	–	0.1602	0.2063	0.2037	0.1532	0.2017	0.1520	0.0657
Λ_f	1	0.7542	0.8453	0.8489	0.8826	0.8517	0.8841	0.6991
Ω	∞	4.7066	4.0981	4.1684	5.7630	4.2235	5.8185	10.6399

carrying capacity amongst all the studied bearing geometries. However, it is interesting to note that the partially textured contact with rectangular features provides a relatively comparable load carrying capacity. The contact with triangular textures is only comparable with the inclined pad bearing's performance. Nevertheless, the favourable comparisons between the textured surfaces and the traditionally established bearing geometries show the fidelity and relevance of surface texturing. Clearly, the traditional bearing geometries cannot be used to a host of applications, such as for the piston compression ring [2,7,14,23,36] or piston skirts or cylinder liners [4,37], highlighted here, where reduced frictional losses have been reported.

It is noteworthy that the results of the current study are limited to the hydrodynamic regime of lubrication. In addition, the current analysis does not include the effect of thermal distortion of contiguous contacting solids or their localised elastic deformation, which can affect the conjunctional geometry of the bearing and that of the textures themselves. Therefore, at high loads, small clearances and high values of relative surface velocities; thus generated heat, different optimal designs might be sought.

6. Closing remarks

The performance of partially textured sliding surfaces with larger than the minimum film thickness.

In the case of parabolic converging-diverging conjunctions, the optimum crown-height is found to be approximately 20% larger than the minimum film thickness. In addition, an empirical relationship is provided for determining the location of lubricant film rupture and commencement of the cavitation zone.

Future work should include the application of the expounded approach to the case of textured pad bearings as an interesting problem with wide-ranging application. Furthermore, the spatial variation of texture features along a bearing length may present further opportunities for optimisation.

Acknowledgement

The authors would like to express their gratitude to the UK Engineering and Physical Sciences Research Council (EPSRC) (EP/G012334/1) for the funding of the Encyclopaedic Program Grant (www.Encyclopaedic.org), under which some of the reported research was carried out.

Appendix

The dimensionless form of Reynolds equation under steady state condition (i.e. with no squeeze film effect) for an incompressible iso-viscous fluid in one-dimension is:

$$\frac{\partial}{\partial \bar{x}}\left(\bar{h}^3\frac{\partial \bar{p}}{\partial \bar{x}}\right) = 6\frac{\partial \bar{h}}{\partial \bar{x}} \tag{I}$$

where, the dimensionless form of pressure and film profile are: $\bar{p} = ph_0^2/\eta UL$ and $\bar{h} = h/h_0$. In addition, the dimensionless axial coordinate is: $\bar{x} = x/L$.

This yields:

$$\overline{p}(\overline{x}) = 6\left(\int_{-1/2}^{\overline{x}} \frac{1}{\overline{h}^2} d\overline{s} - \overline{h}_c \int_{-1/2}^{\overline{x}} \frac{1}{\overline{h}^3} d\overline{s}\right) \tag{II}$$

where, $\overline{h}_c$ is the dimensionless form of contact height at the cavitation inception point (lubricant film rupture position).

Using Swift-Stieber boundary conditions: $(\partial\overline{p}/\partial\overline{x})_{\overline{x}=\overline{c}} = \overline{p}(\overline{c}) = 0$, and solving the following equation, the location of the cavitation inception point can be determined:

$$\int_{-1/2}^{\overline{c}} \frac{1}{\overline{h}^2} d\overline{x} = \overline{h}_c \int_{-1/2}^{\overline{c}} \frac{1}{\overline{h}^3} d\overline{x} \tag{III}$$

This results in the non-linear equation (28) for a converging-diverging parabolic conjunction.

Once the pressure distribution is found, the dimensionless form of load carrying capacity is obtained as:

$$\Lambda_w = \frac{W}{\eta U}\left(\frac{h_m}{L}\right)^2 = \int_{-1/2}^{\overline{c}} \overline{p}(\overline{x}) d\overline{x} \tag{IV}$$

which, results in equation (27) for a parabolic converging-diverging profile.

Furthermore, the viscous shear in both cavitated and full-film contacting regions are obtained as:

$$\overline{\tau} = \frac{h_m}{\eta U}\tau = \begin{cases} \pm\dfrac{\overline{h}}{2}\dfrac{\partial\overline{p}}{\partial\overline{x}} + \dfrac{\overline{U}}{\overline{h}}, & -\dfrac{1}{2} \le \overline{x} < \overline{c} \\ \dfrac{\overline{U}}{\overline{h}}, & \overline{c} \le \overline{x} \le +\dfrac{1}{2} \end{cases} \tag{V}$$

where, $\overline{c} = c/L$ is the dimensionless cavitation inception point and $\overline{U} = (U_2 - U_1)/(U_2 + U_1)$ is an indicative of the slide-roll ratio.

Finally, the dimensionless viscous friction becomes:

$$\Lambda_f = \frac{f}{\eta U}\left(\frac{h_m}{L}\right) = \int_{-1/2}^{1/2} \overline{\tau} d\overline{x} \tag{VI}$$

which, substituting the relevant parameters would result in equation (30).

References

[1] Etsion I, Burstein L. A model for mechanical seals with regular microsurface structure. Tribol Trans 1996;39(3):677–83.

[2] Etsion I, Kligerman Y, Halperin G. Analytical and experimental investigation of laser-textured mechanical seal faces. Tribol Trans 1999;42(3):511–6.

[3] Ronen A, Etsion I, Kligerman Y. Friction-reducing surface-texturing in reciprocating automotive components. Tribol Trans 2001;44(3):359–66.

[4] Rahnejat H, Balakrishnan S, King PD, Howell-Smith S. In-cylinder friction reduction using a surface finish optimization technique. Proc IMechE, Part D J Automob Eng 2006;220(9):1309–18.

[5] Morris NJ, Leighton M, Rahmani R, De la Cruz M, Rahnejat H. Friction reduction in piston ring cylinder liner contact using textured surfaces. Manchester, UK: LUBMAT; 2014. Paper number: L14ICE068, 8pp.

[6] Morris N, Leighton M, De la Cruz M, Rahmani R, Rahnejat H, Howell-Smith S. Combined numerical and experimental investigation of the micro-hydrodynamics of chevron-based textured patterns influencing conjunctional friction of sliding contacts. Proc IMechE, Part J: J Eng Tribol 2015;229(4):316–35.

[7] Kovalchenko AM, Erdemir A, Ajayi OO, Etsion I. Tribological behavior of oil-lubricated laser textured steel surfaces in conformal flat and non-conformal contacts. Mater Perform Charact 2017;6(2):1–23.

[8] Sinanoglu C, Nair F, Karamis B. Effects of shaft surface texture on journal bearing pressure distribution. J Mater Process Technol 2005;168(2):344–53.

[9] Tala-Ighil N, Fillon M, Maspeyrot P. Effect of textured area on the performances of a hydrodynamic journal bearing. Tribol Int 2011;44(3):211–9.

[10] Morris NJ, Rahmani R, Rahnejat H. Tribology of partial pad journal bearings with textured surfaces. Vienna, Austria. In: 3rd european conf. On tribology (ECOTRIB 2011); June 7-9, 2011. http://dx.doi.org/10.13140/RG.2.1.1219.7926.

[11] Tala-Ighil N, Fillon M. Performance evolution of fully and partially textured hydrodynamic journal bearings lubricated with two lubricants. IOP Conf Ser Mater Sci Eng 2017;174(1):012032.

[12] Etsion I, Halperin G, Brizmer V, Kligerman Y. Experimental investigation of laser surface textured parallel thrust bearings. Tribol Lett 2012;17(2):295–330.

[13] Zouzoulas V, Papadopoulos CI. 3-D thermohydrodynamic analysis of textured, grooved, pocketed and hydrophobic pivoted-pad thrust bearings. Tribol Int 2017;110:426–40.

[14] Ryk G, Kligerman Y, Etsion I. Experimental investigation of laser surface texturing for reciprocating automotive components. Tribol Trans 2002;45(4):444–9.

[15] Garbon W, Pawlus P, Wos S, Koszela W, Wieczorowski M. Effects of honed cylinder liner surface texture on tribological properties of piston ring-liner assembly in short time tests. Tribol Int 2017;113:137–48.

[16] Adjemout M, Andrieux A, Bouyer J, Brunetiere N, Marcos G, Czerwiec T. Influence of the real dimple shape on the performance of a textured mechanical seal. Tribol Int 2017;115:409–16.

[17] Pettersson U, Jacobson S. Friction and wear properties of micro textured DLC coated surfaces in boundary lubricated sliding. Tribol Lett 2004;17(3):553–9.

[18] Bhardwaj V, Pandey RK, Agarwal VK. Experimental investigations for tribo-dynamic behaviours of conventional and textured races ball bearings using fresh and MoS2 blended greases. Tribol Int 2017;113:149–68.

[19] Shinde AB, Pawar PM. Multi-objective optimization of surface textured journal bearing by Taguchi based Grey relational analysis. Tribol Int 2017;114:349–57.

[20] Dobrica MB, Fillon M, Pascovici MD, Cicone T. Optimizing surface texture for hydrodynamic lubricated contacts using a mass-conserving numerical approach. Proc IMechE, Part J J Eng Tribol 2010;224(8):737–50.

[21] Papadopoulos CI, Efstathiou EE, Nikolakopoulos PG, Kaiktsis I. Geometry optimization of textured three-dimensional micro-thrust bearings. Trans ASME, J Tribol 2011;133(4):041702.

[22] Papadopoulos CI, Nikolakopoulos PG, Kaiktsis L. Evolutionary optimization of micro-thrust bearings with periodic partial trapezoidal surface texturing. Trans ASME, J Eng Gas Turbines Power 2011;133(1):012301.

[23] Morris NJ, Rahmani R, Rahnejat H. A hydrodynamic flow analysis for optimal positioning of surface textures. Proc IMechE, Part J J Eng Tribol 2017. http://dx.doi.org/10.1177/1350650117709672.

[24] Rahmani R, Shirvani A, Shirvani H. Optimization of partially textured parallel thrust bearings with square-shaped micro-dimples. Tribol Trans 2007;50(3):401–6.

[25] Rahmani R, Mirzaee I, Shirvani A, Shirvani H. An analytical approach for analysis and optimisation of slider bearings with infinite width parallel textures. Tribol Int 2010;43(8):1551–65.

[26] Rahmani R. An investigation into analysis and optimisation of textured slider bearings with application in piston-ring/cylinder liner contact. PhD Thesis. UK: Anglia Ruskin University; 2008.

[27] Rahmani R, Shirvani A, Shirvani H. Optimised textured surfaces with application in piston-ring/cylinder liner contact. In: Rahnejat H, editor. Tribology and dynamics of engine and powertrain: fundamentals, applications and future trends. UK: Woodhead Publishing Ltd; 2010. p. 470–517. http://dx.doi.org/10.13140/RG.2.1.3316.9447.

[28] Gropper D, Wang L, Harvey TJ. Hydrodynamic lubrication of textured surfaces: a review of modeling techniques and key findings. Tribol Int 2016;94:509–29.
[29] Morris N, Rahmani R, Rahnejat H, King PD, Fitzsimons B. Tribology of piston compression ring conjunction under transient thermal mixed regime of lubrication. Tribol Int 2013;59:248–58.
[30] Shahmohamadi H, Rahmani R, Rahnejat H, Garner CP, Dowson D. Big end bearing losses with thermal cavitation flow under cylinder deactivation. Tribol Lett 2015; 57(2):1–17.
[31] Paouris L, Rahmani R, Theodossiades S, Rahnejat H, Hunt G, Barton W. An analytical approach for prediction of elastohydrodynamic friction with inlet shear heating and starvation. Tribol Lett 2016;64(10):1–18.
[32] Rahmani R, Shirvani A, Shirvani H. Analytical analysis and optimisation of the Rayleigh step slider bearing. Tribol Int 2009;42(5):666–74.
[33] Morris N, Rahmani R, Rahnejat H, King PD, Fitzsimons B. The influence of piston ring geometry and topography on friction. Proc IMechE, Part J J Eng Tribol 2013; 227(2):141–53.
[34] Gore M, Morris N, Rahmani R, Rahnejat H, King PD, Howell-Smith S. A combined analytical-experimental investigation of friction in cylinder liner inserts under mixed and boundary regimes of lubrication. Lubr Sci 2017. http://dx.doi.org/10.1002/ls.1369.
[35] Gohar R, Rahnejat H. Fundamentals of tribology. London: Imperial College Press; 2008.
[36] Etsion I. Surface texturing for in-cylinder friction reduction. In: Rahnejat H, editor. Tribology and dynamics of engine and powertrain: fundamentals, applications and future trends. UK: Woodhead Publishing Ltd.; 2010. p. 458–69. http://dx.doi.org/10.13140/RG.2.1.3316.9447.
[37] Howell-Smith S, Rahnejat H, King PD, Dowson D. Reducing in-cylinder parasitic losses through surface modification and coating. Proc IMechE, Part D J Automob Eng 2014;228(4):391–402.

Nomenclature

c: location of cavitation inception point (lubricant film rupture point)
d_x: length of texture feature
f: friction per unit lateral width
h: contact profile (film thickness)
h_d: maximum depth of texture feature
h_i: maximum inclination height
h_m: minimum film thickness
h_r: crown height of parabolic profile
h_s: . step height
L: total length of contact
l_0: leading edge of the textured surface
l_n: trailing edge of the textured surface
l_s: step length
l_x: interspatial spacing of textures (i.e. edge-to-edge distance)
m: number of textures
p: hydrodynamic pressure
R: radius of curvature of the parabolic profile
$\bar{s}$: an intermediate integration variable
U: sliding velocity
$\overline{U}$: indicative slide-roll ratio
W: load carrying capacity per unit lateral width
x, y, z: Cartesian frame of referenceGreek symbols
α_0: leading edge ratio for the textured surface
α_n: trailing edge ratio for the textured surface
ε: texture length ratio
η: dynamic viscosity of the lubricant
θ: inclination angle
κ: textured length ratio, step length ratio
Λ_f: dimensionless friction
Λ_w: dimensionless load carrying capacity
λ: Stribeck lubricant film ratio
μ: coefficient of friction
ξ: texture depth ratio, height ratio parameter, step ratio
σ: composite RMS roughness of counter face surfaces
τ: viscous shear stress
Ω: scaled coefficient of frictionAbbreviations
CAS: Computer Algebra System
LST: Laser Surface Texturing
max: maximum
min: minimum
opt: optimum
RMS: Root Mean Square